

1 INTRODUCTION

2 Above Earth's atmosphere are the a pair of Van Allen radiation belts, a complex  
3 and dynamic plasma environment that effects our technology-driven society. These  
4 effects include: a higher radiation dose for astronauts and cosmonauts, higher chance  
5 of spacecraft failure due to single event upsets that can lead to catastrophic latchups,  
6 degradation of silicon (changing the silicon doping) from an extended radiation dose  
7 that can degrade a transistor to the point where it no longer function as a switch,  
8 and the degradation of the ozone layer due to the chemical production of  $\text{NO}_X$  and  
9  $\text{HO}_X$  molecules. With these effects in mind, it is no surprise that the radiation belts  
10 have been extensively studied since their discovery in the 1960s.

11 One natural phenomenon in the radiation belts that has been a topic of interest  
12 in the space physics community is wave-particle intersections that, as we will explore  
13 throughout this dissertation, can accelerate particles to very high energies (e.g.  $\approx$   
14 MeV for electrons) and scatter them into the atmosphere.

15 The goal of this dissertation is to study the wave-particle mechanism that  
16 scatters microbursts, a sub-second impulse of electrons into Earth's atmosphere.  
17 Before we dive deep into the physics of wave-particle interactions, an introduction to  
18 Earth's magnetosphere is warranted. Single charged particle motion in Earth's electric  
19 and magnetic fields will be described first. Then the major particle populations in  
20 the magnetosphere and the coupling between them will be described. Lastly, a brief  
21 overview of wave-particle interactions and their effects will be presented.

22 Charged Particle Motion in Electric and Magnetic Fields

A charged particle trapped in the magnetosphere will experience three types  
of periodic motion in Earth's nearly dipolar magnetic field. The three motions are

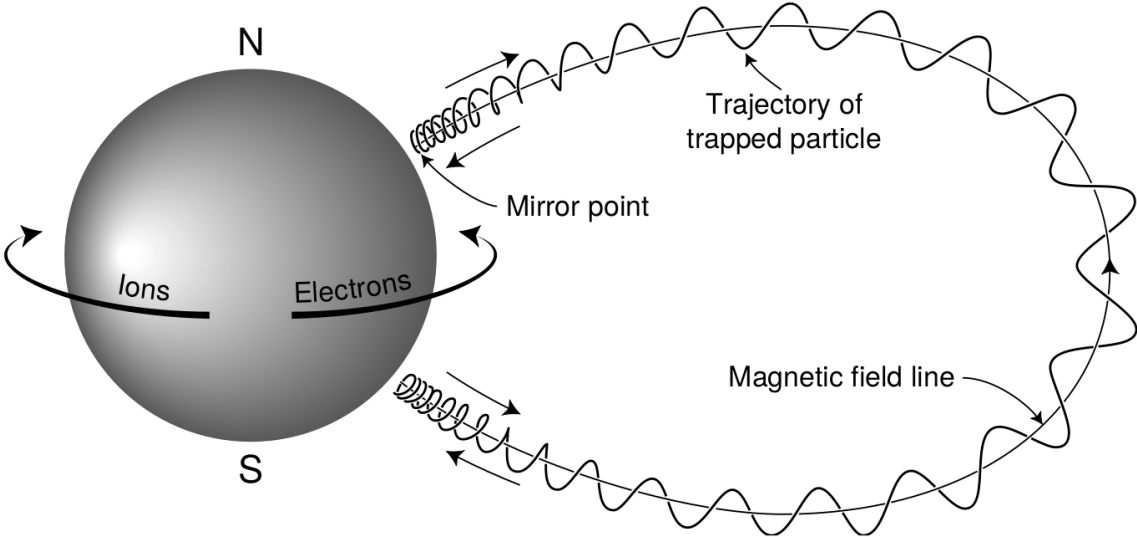


Figure 1.1: The three periodic motions of charged particles in Earth's dipole magnetic field. These motions are: gyration about the magnetic field line, bounce motion between the magnetic poles, and azimuthal drift around the Earth. Figure from (Baumjohann and Treumann, 1997).

ultimately due to the Lorentz force that a particle of momentum  $\vec{p}$ , charge  $q$ , and velocity  $\vec{v}$  experiences in an electric field  $\vec{E}$  and magnetic field  $\vec{B}$  and is given by

$$\frac{d\vec{p}}{dt} = q(\vec{E} + \vec{v} \times \vec{B}). \quad (1.1)$$

- <sup>23</sup> In the magnetosphere, the three periodic motions in decreasing frequency are gyration,
- <sup>24</sup> bounce, and drift and are schematically shown in Fig. 1.1. Each of periodic these
- <sup>25</sup> motions have a corresponding conserved quantity i.e. an adiabatic invariant.

The highest frequency periodic motion is gyration about a magnetic field of magnitude  $B$ . This motion is circular with a Larmor radius of

$$r = \frac{mv_{\perp}}{|q|B} \quad (1.2)$$

where  $m$  is the mass and  $v_{\perp}$  the particle's velocity perpendicular to  $\vec{B}$ . This motion

has a corresponding gyrofrequency

$$\Omega = \frac{|q|B}{m} \quad (1.3)$$

in units of radians/second. Inside the radiation belts the electron gyrofrequency,  $\Omega_e$  is on the order of a kHz. The corresponding adiabatic invariant is found by integrating the particle's canonical momentum around the particle's path of gyration

$$J_i = \oint (\vec{p} + q\vec{A}) \cdot d\vec{l} \quad (1.4)$$

where  $J_i$  is the  $i^{th}$  adiabatic invariant and  $\vec{A}$  is the magnetic vector potential. This integral is carried out by integrating the first term over the circumference of the gyro orbit and integrating the second term using Stokes theorem to calculate the magnetic flux enclosed by the gyro orbit. With suitable integration,  $J_1 \sim v_{\perp}^2/B$  and is conserved as the frequency of the driving force,  $\omega$  satisfies  $\omega \ll \Omega_e$ .

The second highest frequency periodic motion is bouncing due to a parallel gradient in  $\vec{B}$ . This periodic motion naturally arises in the magnetosphere because Earth's magnetic field is stronger near the poles, and artificially in the laboratory in magnetic bottle machines. To understand this motion we first need to define the concept of pitch angle  $\alpha$  as the angle between  $\vec{B}$  and  $\vec{v}$  which is schematically shown in Fig. 1.2a. The pitch angle relates  $v$  with  $v_{\perp}$ , and  $v_{\parallel}$  (the component of the particles velocity parallel to  $\vec{B}$ ). As shown in 1.2b and c, a larger  $\alpha$  will tighten the particle's helical trajectory and vice versa.

Assuming the particle's kinetic energy is concerned, the conservation of  $J_1$  implies that given a particle's  $v_{\perp}(0)$  and  $B(0)$  at the magnetic equator (where Earth's magnetic field is usually at a minimum), we can calculate its  $v_{\perp}(s)$  along the particle's path  $s$  by calculating  $B(s)$  from magnetic field models. The particle's perpendicular

velocity is then related via

$$\frac{v_{\perp}^2(0)}{B(0)} = \frac{v_{\perp}^2(s)}{B(s)} \quad (1.5)$$

<sup>39</sup> which can be rewritten as

$$\frac{v^2 \sin^2 \alpha(0)}{B(0)} = \frac{v^2 - v_{\parallel}^2(s)}{B(s)} \quad (1.6)$$

<sup>40</sup> and re-arranged to solve for  $v_{\parallel}(s)$

$$v_{\parallel}(s) = v \sqrt{1 - \frac{B(s)}{B(0)} \sin^2 \alpha(0)} \quad (1.7)$$

<sup>41</sup> which will tend towards 0 when the second term in the radical approaches 1.

<sup>42</sup> The location where  $v_{\parallel}(s) = 0$  is called the mirror point and is where a particle  
<sup>43</sup> stops and reverses direction. Since Earth's magnetic field is stronger towards the  
<sup>44</sup> poles, the mirroring particle will execute periodic bounce motion between its two  
<sup>45</sup> mirror points in the northern and southern hemispheres. The corresponding adiabatic  
<sup>46</sup> invariant,  $J_2$  is

$$J_2 = \oint p_{\parallel} ds \quad (1.8)$$

where  $ds$  describes the particle path between the mirror points in the northern and southern hemispheres (see Fig. 1.1).  $J_2$  is found by substituting Eq. 1.7 into Eq. 1.8 and defining the magnetic field strength at the mirror points as  $B_m$  where  $\alpha(m) = 90^\circ$ .

The  $J_2$  integral can be written as

$$J_2 = 2p \int_{m_n}^{m_s} \sqrt{1 - \frac{B(s)}{B(m)}} ds \quad (1.9)$$

<sup>47</sup> where  $m_n$  and  $m_s$  are the northern and southern mirror points, respectively. The

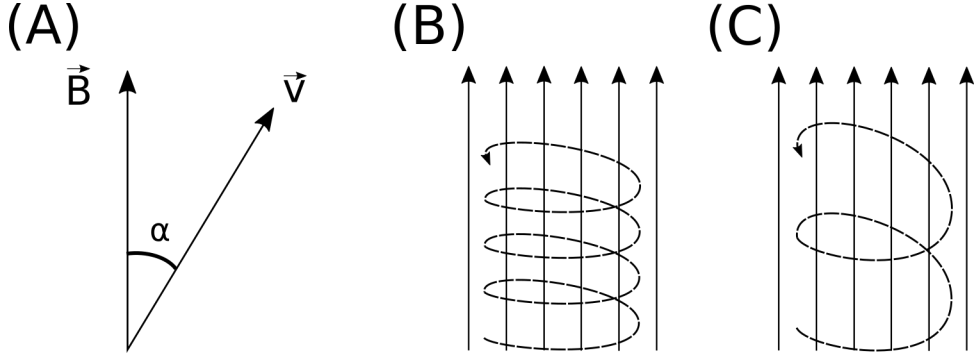


Figure 1.2: Charged particle motion in a uniform magnetic field  $\vec{B}$ . Panel (A) shows the geometry defining the pitch angle,  $\alpha$ . Panel (B) and (C) show two helical electron trajectories with dashed lines assuming a large and small  $\alpha$  (corresponding to a small and large parallel velocity  $v_{||}$ ), respectively.

<sup>48</sup> bounce period can be estimated (e.g. Baumjohann and Treumann, 1997) to be

$$t_b \approx \frac{LR_e}{\sqrt{W/m}}(3.7 - 1.6 \sin \alpha(0)) \quad (1.10)$$

<sup>49</sup> where  $L$  is the  $L$ -shell which describes the distance from the Earth's center to the  
<sup>50</sup> location where a particular magnetic field line crosses the magnetic equator, in units  
<sup>51</sup> of Earth radii,  $R_e$ .  $W$  is the particle's kinetic energy. As with gyration, a particle  
<sup>52</sup> bounces as long as  $\omega \ll \Omega_b$ , where  $\Omega_b$  is the bounce frequency.

<sup>53</sup> At this stage it is instructional to introduce the notion of the loss cone pitch  
<sup>54</sup> angle,  $\alpha_L$ . A particle with  $\alpha \leq \alpha_L$  will mirror at or below  $\approx 100$  km altitude in the  
<sup>55</sup> atmosphere. A particle at those altitudes will encounter Earth's atmosphere and has  
<sup>56</sup> a significant probability of Coulomb scattering with atmospheric particles and be lost  
<sup>57</sup> to the atmosphere.

<sup>58</sup> The slowest periodic motion experienced by charged particles in Earth's mag-  
<sup>59</sup> netic field is azimuthal drift around the Earth. This drift results from a combination of  
<sup>60</sup> a radial gradient in  $\vec{B}$  and the curvature of the magnetic field. The radial gradient drift  
<sup>61</sup> arises because Earth's magnetic field is stronger near the Earth where the particle's

62 gyroradius radius of curvature is smaller as it gyrates towards stronger magnetic field,  
 63 and larger when it gyrates outward. The overall effect is the particle gyro orbit does  
 64 not close on itself and negatively charged particles drift East and positively charged  
 65 particles drift West. The radial gradient drift is enhanced by the centrifugal force that  
 66 a particle experiences as it bounces along the curved field lines. The drift adiabatic  
 67 invariant,  $J_3$  is found by integrating Eq. 1.4 over the complete particle orbit around  
 68 the Earth. The shape of this drift orbit is otherwise known as a drift shell. For  $J_3$ ,  
 69 the first term is negligible and the second term is the magnetic flux enclosed by the  
 70 drift shell,  $\Phi_m$  i.e.  $J_3 \sim \Phi_m$ .

71 Figure 1.3 from Schulz and Lanzerotti (1974) shows contours of the gyration,  
 72 bounce, and drift frequencies for electrons and protons in Earth's dipole magnetic  
 73 field.

Up until now we have considered the three periodic motions due Earth's magnetic field and the absence of electric fields. If  $\vec{E}$  is present, a particle's center of gyration i.e., averaged position of the particle over a gyration, will drift with a velocity perpendicular to both  $\vec{E}$  and  $\vec{B}$ . The drift velocity can be solved directly from Eq. 1.1 and is

$$\vec{v}_E = \frac{\vec{E} \times \vec{B}}{B^2}. \quad (1.11)$$

74 Lastly, for more detailed derivations of these motions, see the following texts:  
 75 Baumjohann and Treumann (1997); Schulz and Lanzerotti (1974); Tsurutani and  
 76 Lakhina (1997).

77 Particle Populations and Their Interractions in the Magnetosphere

78 The single-particle motion in Earth's magnetic field described in the previous  
 79 section is a prerequisite to understanding how magnetospheric particles organize into

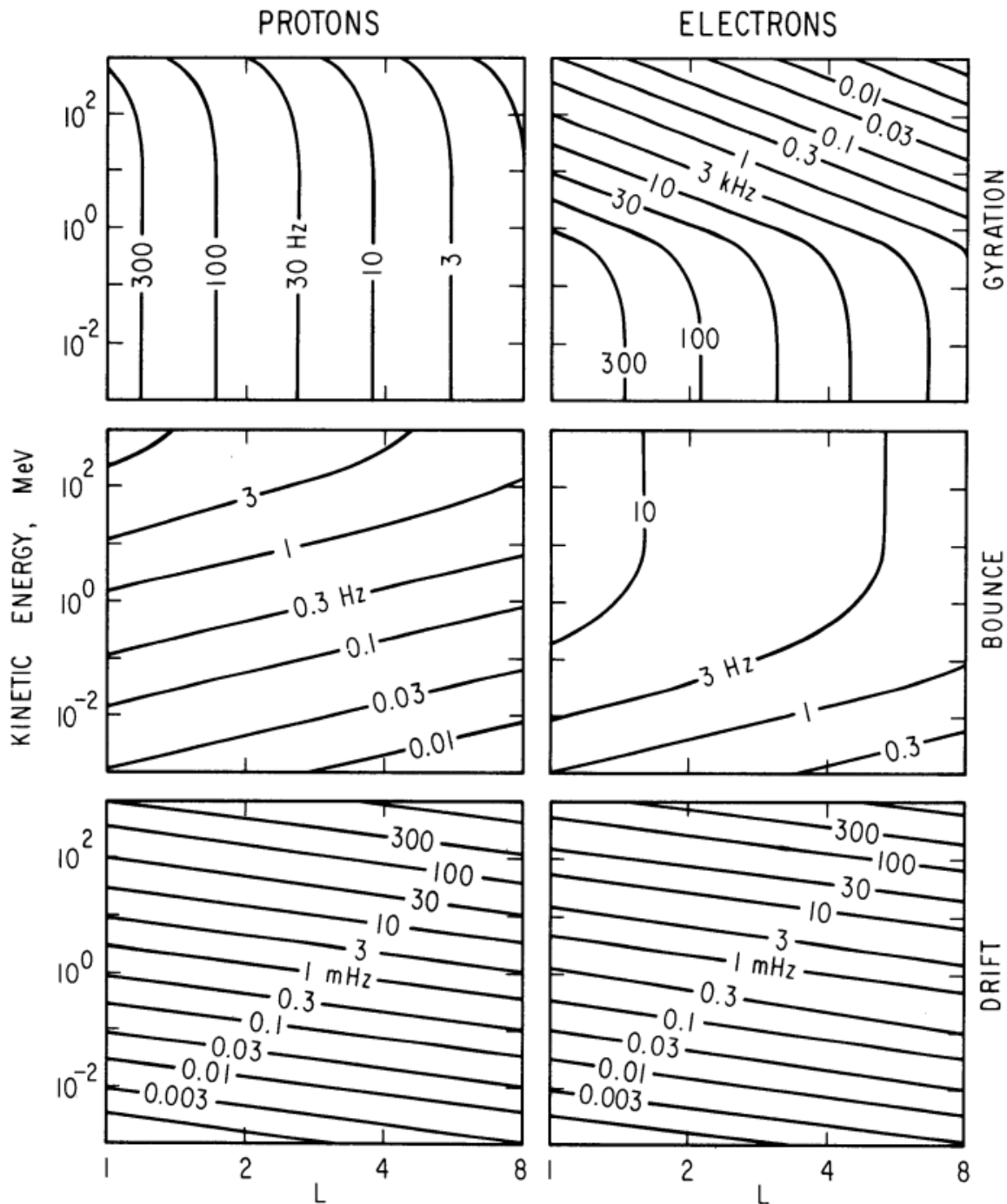


Figure 1.3: Contours of constant gyration, bounce, and drift frequencies for electrons and protons in a dipole field. Figure from Schulz and Lanzerotti (1974).

macroscopic populations. The structure of the outer magnetosphere is shown in Fig. 1.4 and inner magnetosphere in Fig. 1.5. In this section we will introduce the various particle populations in the magnetosphere and how they couple.

The sun and its solar wind are ultimately the source of energy input into the magnetosphere. The solar wind at Earth's orbit is a plasma traveling at supersonic speeds with an embedded interplanetary magnetic field (IMF). When the solar wind encounters Earth's magnetic field the plasma can not easily penetrate into the magnetosphere, rather it drapes around the magnetosphere forming a cavity in the solar wind that is roughly shaped as shown in Fig. 1.4. Because the solar wind is supersonic at 1 AU, a bow shock exists upstream of the magnetosphere. The solar wind plasma, after it is shocked by the bow shock, flows around the magnetosphere inside the magnetosheath. The surface where the solar wind ram pressure and Earth's magnetic pressure balance is termed the magnetopause, which can be thought of as a boundary between the solar wind's and Earth's plasma environments. This is a slightly naive description of the magnetopause, but is nonetheless an instructive conceptual picture. The shocked plasma then flows past the Earth where it shapes the magnetotail. In the magnetotail the solar wind magnetic pressure balances Earth's magnetic field pressure in the lobes. The magnetotail extends on the order of 100  $R_E$  downstream of Earth [Add citation](#), and the tailward stretching of magnetic field lines creates the plasma sheet which exists in the region of low magnetic field strength near the magnetic equator [Add citation](#). The plasma sheet flows from dusk to dawn (out of the page in Figs. 1.4 and 1.5) and this current is connected to a zoo of other currents in the magnetosphere which is beyond the scope of this dissertation.

The idea of the magnetopause as a barrier between the solar wind and the magnetosphere is not entirely accurate due to the presence of reconnection. Reconnection was first conceived by Dungey (1961) who described the convection of

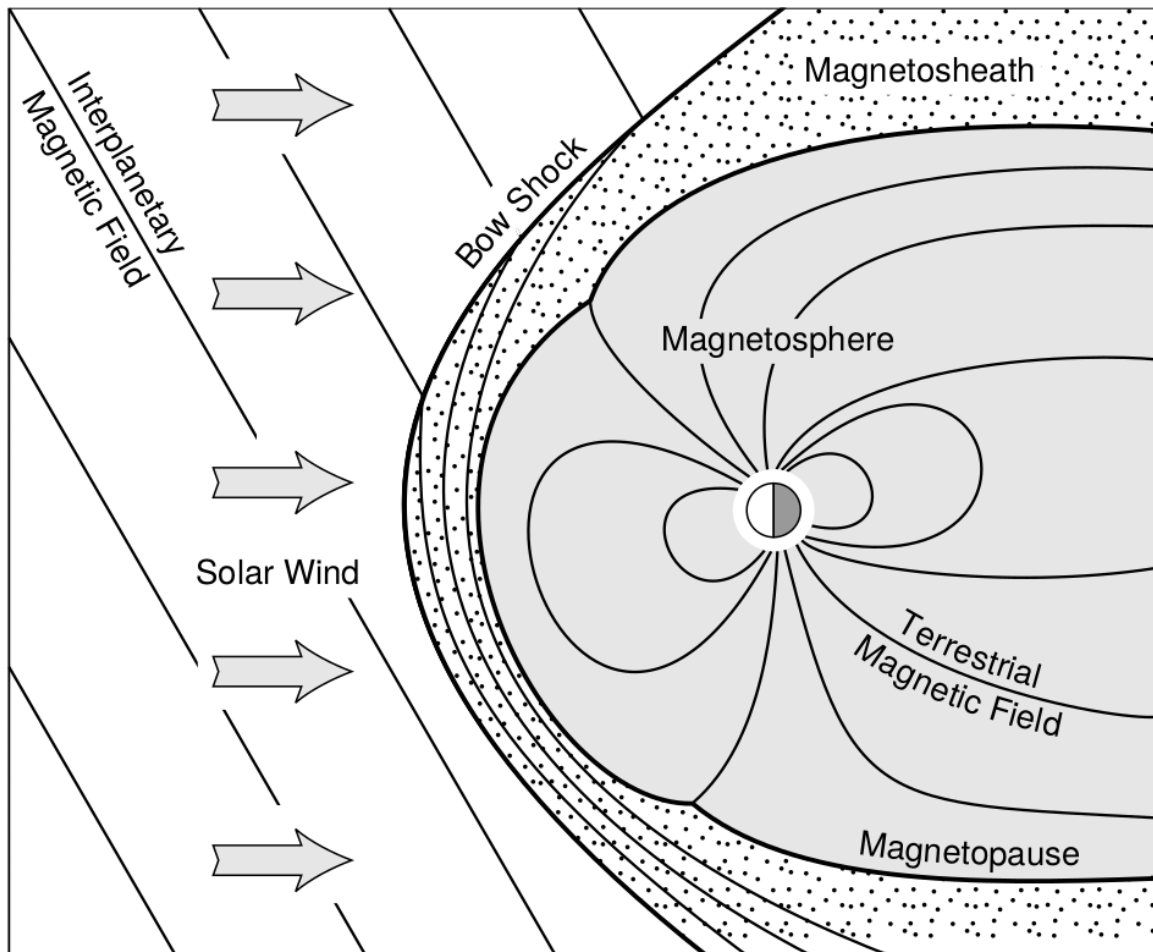


Figure 1.4: Macroscopic structures in the outer magnetosphere. The solar wind with its frozen-in interplanetary magnetic field is shown on the left and is traveling supersonically towards the right. The solar wind envelops Earth's magnetic field to create the magnetosphere cavity. Since the solar wind is traveling supersonically, it creates a bow shock up stream. Downstream of the bow shock the shocked solar wind plasma inside the magnetosheath flows around the magnetopause, a boundary between the solar wind and magnetosphere. Figure from Baumjohann and Treumann (1997).

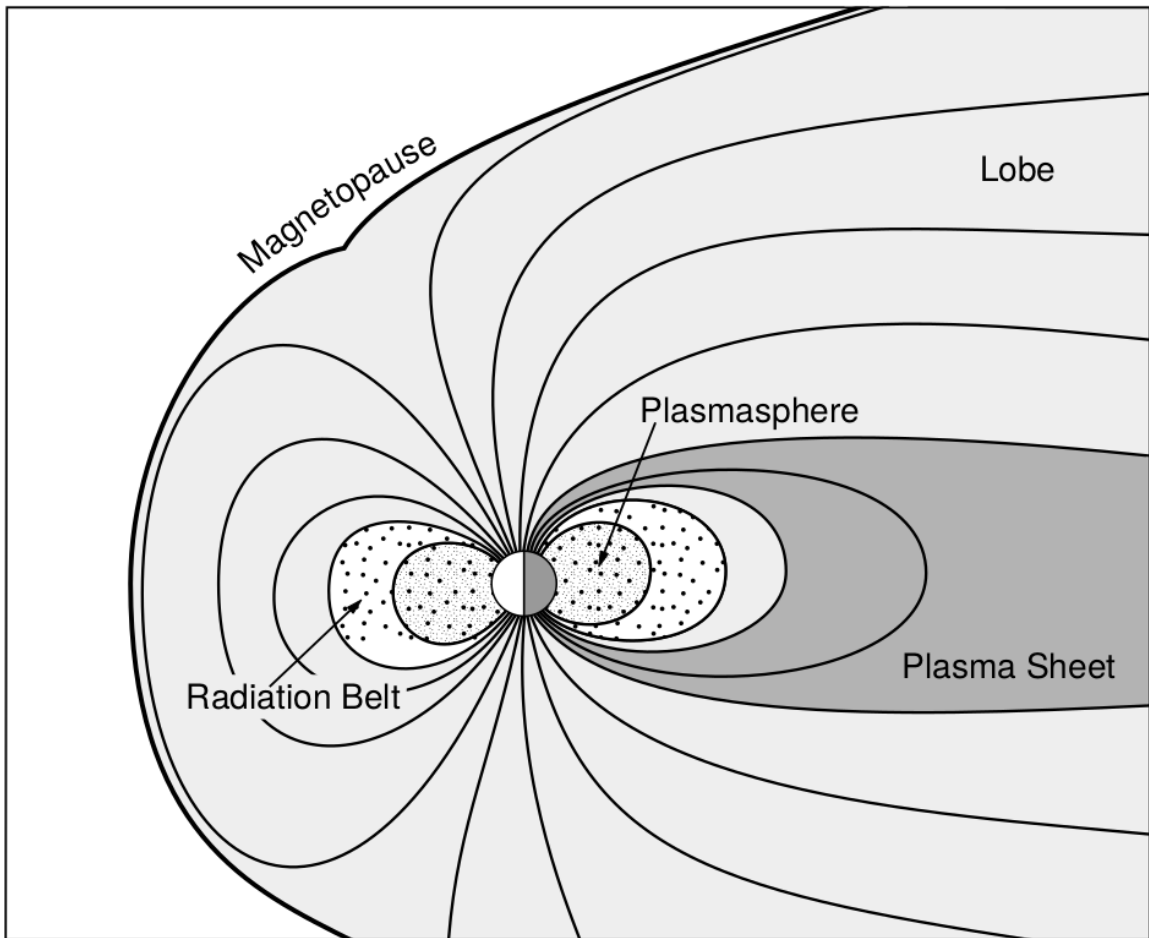


Figure 1.5: Macroscopic structures in the inner magnetosphere most relevant to this dissertation. The plasmasphere, and the radiation belts are shown and ring current is co-located there as well. Sun is to the left. Figure from Baumjohann and Treumann (1997).

106 Earth's magnetic field between the bow and tail regions of the magnetosphere. This  
 107 process is known as the Dungey cycle and is most effective when the IMF is pointing  
 108 southward as is shown in Fig. 1.6 part 1. As the IMF contacts Earth's magnetic  
 109 field it reconnects with it so that Earth's magnetic field is directly connected to the  
 110 IMF. Then as the solar wind flows tailward the IMF drags Earth's magnetic field  
 111 towards the magnetotail as shown in Fig. 1.6 parts 2-6. As more and more magnetic  
 112 field lines are draped in the magnetotail, magnetic pressure increases in the lobes  
 113 which squeezes the plasma sheet until Earth's magnetic field reconnects as is shown  
 114 in Fig. 1.6 part 7. Lastly, Fig. 1.6 part 8 shows the newly merged magnetic field  
 115 line and the plasma frozen on it moves Earthward under the magnetic tension force  
 116 to become more dipolar. This is called a dipolarization of the magnetic field, and the  
 117 plasma frozen on these field lines can be observed as injections (e.g. Turner et al.,  
 118 2015). Injection of plasma into the inner magnetosphere is one of the drivers of inner  
 119 magnetosphere dynamics. **Should I talk about the K-H instability and how there**  
 120 **could be micro reconnection? i.e. cite a paper or two that support or refute that**  
 121 **idea.**

122 Inner Magnetosphere Populations

123 Before we describe the inner magnetosphere particle populations, we first need to  
 124 describe the coordinate system used to organize the inner magnetosphere populations.  
 125 The first coordinate was defined in section 1 and is the L shell. L shell can be thought  
 126 of as an analogue to a radius but in a dipole geometry. The azimuthal coordinate  
 127 is the magnetic local time (MLT). For an observer above Earth's north pole looking  
 128 down, MLT is defined to be 0 (midnight) in the anti-sunward direction, and increases  
 129 in the counter-clockwise direction with 6 at dawn, 12 at noon (sunward direction),  
 130 and 18 in dusk. The last coordinate used in this dissertation is the magnetic latitude,

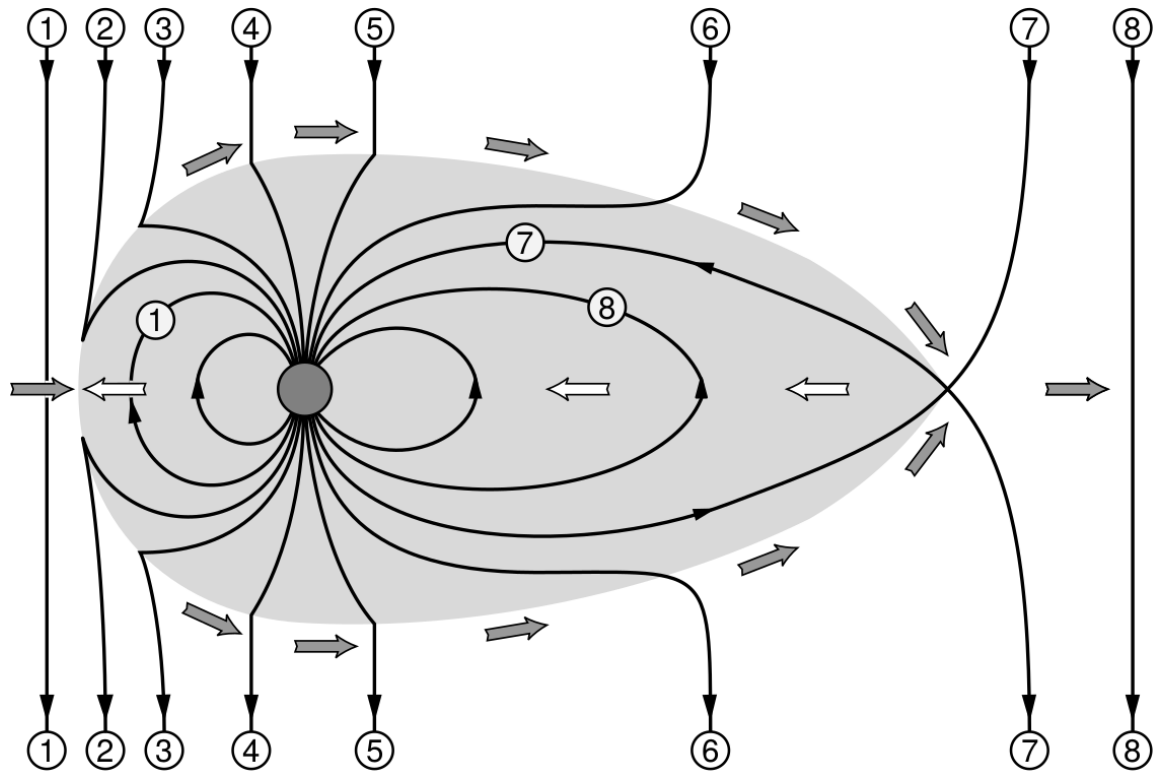


Figure 1.6: The series of steps involved in magnetic reconnection with a southward IMF. Figure from Baumjohann and Treumann (1997).

<sub>131</sub>  $\lambda$  which is analogous to the latitude coordinate and is defined to be 0 at the magnetic  
<sub>132</sub> equator.

<sub>133</sub> The low energy particle dynamics in the inner magnetosphere are organized by  
<sub>134</sub> two electric fields: the co-rotation and the dawn-dusk electric fields. The co-rotation  
<sub>135</sub> electric field arises from the rotation of Earth's magnetic field. Since particles are  
<sub>136</sub> frozen on magnetic field lines and the plasma conductivity is effectively infinite, to  
<sub>137</sub> a non-rotating observer, Earth's rotation appears as a radial electric field that drops  
<sub>138</sub> off as  $\sim L^2$ . This electric field makes particles orbit around the Earth due to the  
<sub>139</sub>  $\vec{E} \times \vec{B}$  drift. The other electric field, pointing from dawn to dusk is called the  
<sub>140</sub> convection electric field and is formed by the Earthward transport of particles from  
<sub>141</sub> the magnetotail that appears as an electric field to a stationary observer (with respect  
<sub>142</sub> to Earth). The superposition of the co-rotation and convection electric fields  
<sub>143</sub> results in a potential field shown in Fig. 1.7. The shaded area in Fig. 1.7 shows  
<sub>144</sub> the orbits on which low energy electrons are trapped, and outside are the untrapped  
<sub>145</sub> particles. The dynamic topology of the shaded region in Fig. 1.7 is controlled by only  
<sub>146</sub> the convection electric field which is dependent on the solar wind speed and the IMF.  
<sub>147</sub> The lowest energy particles, that are most effected by these electric fields, make up  
<sub>148</sub> the plasmasphere.

<sub>149</sub> Plasmasphere The plasmasphere is a dense ( $n_e \sim 10^3/\text{cm}^3$ ), cool plasma  
<sub>150</sub> ( $\sim \text{eV}$ ) that extends to  $L \sim 4$  (extent is highly dependent on the solar wind and  
<sub>151</sub> magnetospheric conditions) and is sourced from the ionosphere. The two main  
<sub>152</sub> mechanisms that source the cold plasma from the ionosphere are ultraviolet ionization  
<sub>153</sub> by sunlight and particle precipitation. The ultraviolet ionization by sunlight is  
<sub>154</sub> strongly dependent on the time of day (day vs night), latitude (more ionization near  
<sub>155</sub> the equator). The ionization due to particle precipitation, on the other hand, is highly

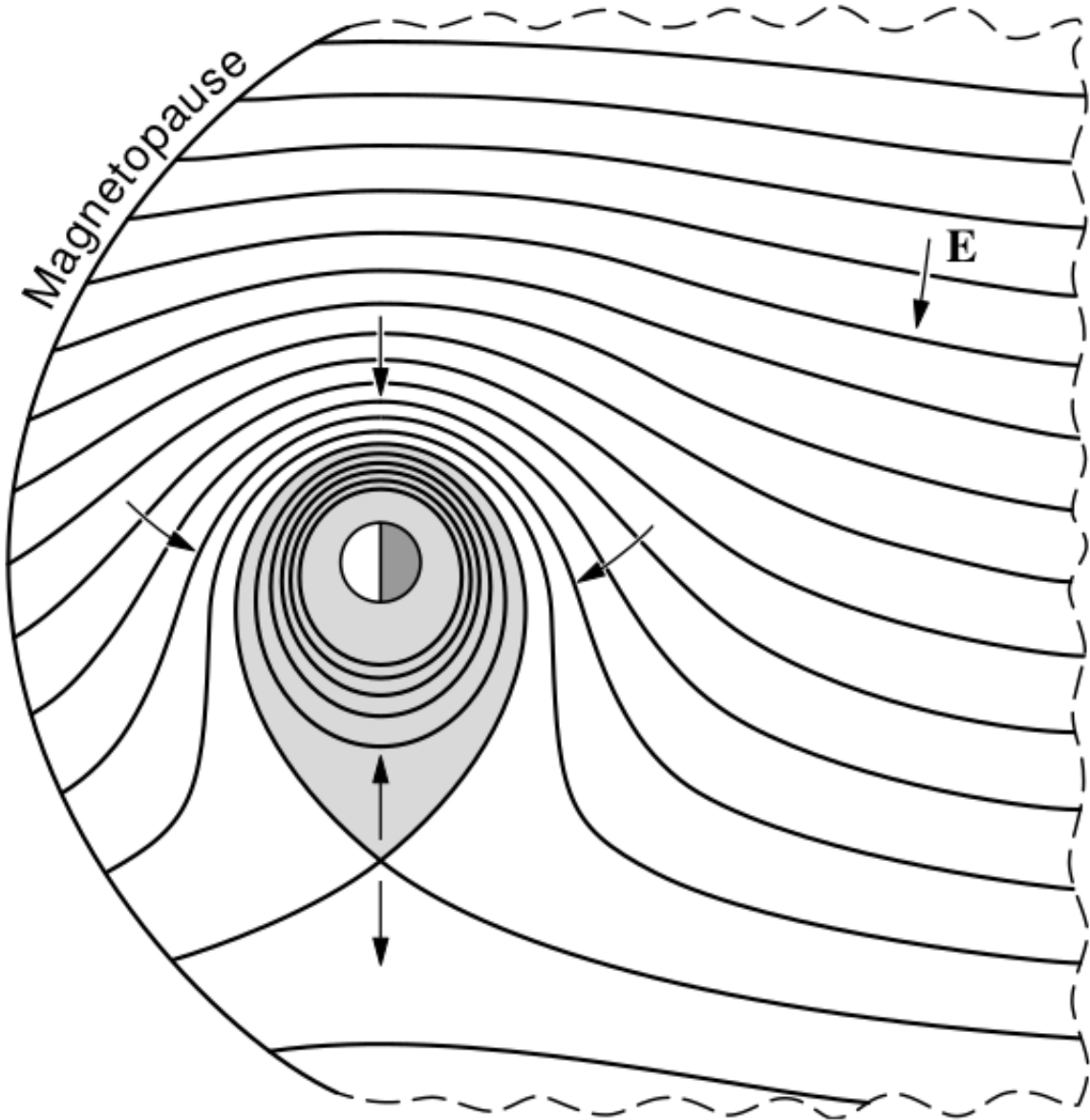


Figure 1.7: Equipotential lines and electric field arrows due to the superposition of the co-rotation and convection electric fields. Electrons in the shaded region execute closed orbits. Outside of the shaded regions the electrons are not trapped and will escape. The region separating the two regimes is called the Alfvén layer. Figure from Baumjohann and Treumann (1997).

<sup>156</sup> dependent on magnetospheric conditions, and mostly occurs at high latitudes.

<sup>157</sup> The outer boundary of the plasmasphere is the plasmapause which is typically  
<sup>158</sup> identified as a steep radial gradient in plasma density from  $\sim 10^3/\text{cm}^3$  to  $\sim 1/\text{cm}^3$ . As  
<sup>159</sup> we will see throughout this dissertation, the location of the plasmapause is important  
<sup>160</sup> to model (e.g. O'Brien and Moldwin, 2003) and understand since the plasma density  
<sup>161</sup> strongly controls the efficiency of particle scattering (Horne et al., 2005).

<sup>162</sup> Ring Current The next higher energy population is the ring current. This  
<sup>163</sup> population consists of protons and electrons between tens and a few hundred keV  
<sup>164</sup> that drift around the Earth. The orbits of higher energy particles are not as effected  
<sup>165</sup> by the convection and co-rotation electric field, rather they drift around the Earth  
<sup>166</sup> due to gradient and curvature drifts. Since the direction of the drift is dependent on  
<sup>167</sup> charge, protons drift west around the Earth and electrons drift East. This has the  
<sup>168</sup> effect of creating a current around the Earth.

<sup>169</sup> The ring current generates a magnetic field which decreases the magnetic field  
<sup>170</sup> strength on Earth's surface and increases it outside of the ring current. The decrease  
<sup>171</sup> of Earth's magnetic field strength is readily observed by a system of ground-based  
<sup>172</sup> magnetometers and is merged into a Disturbance Storm Time (DST) index. An  
<sup>173</sup> example of a DST index time series from a coronal mass ejection (CME) driven 2015  
<sup>174</sup> St. Patrick's Day storm is shown in Fig. 1.8. The ring current is sometimes first  
<sup>175</sup> depleted and DST increases slightly (initial phase or sudden storm commencement).  
<sup>176</sup> Then the ring current is rapidly built up during which DST rapidly decreases (main  
<sup>177</sup> phase). Lastly the ring current gradually decays toward its equilibrium state over a  
<sup>178</sup> period of a few days and DST increases towards 0 (recovery phase). The DST index  
<sup>179</sup> along with other indicies are readily used by the space physics community to quantify  
<sup>180</sup> the global state of the magnetosphere.

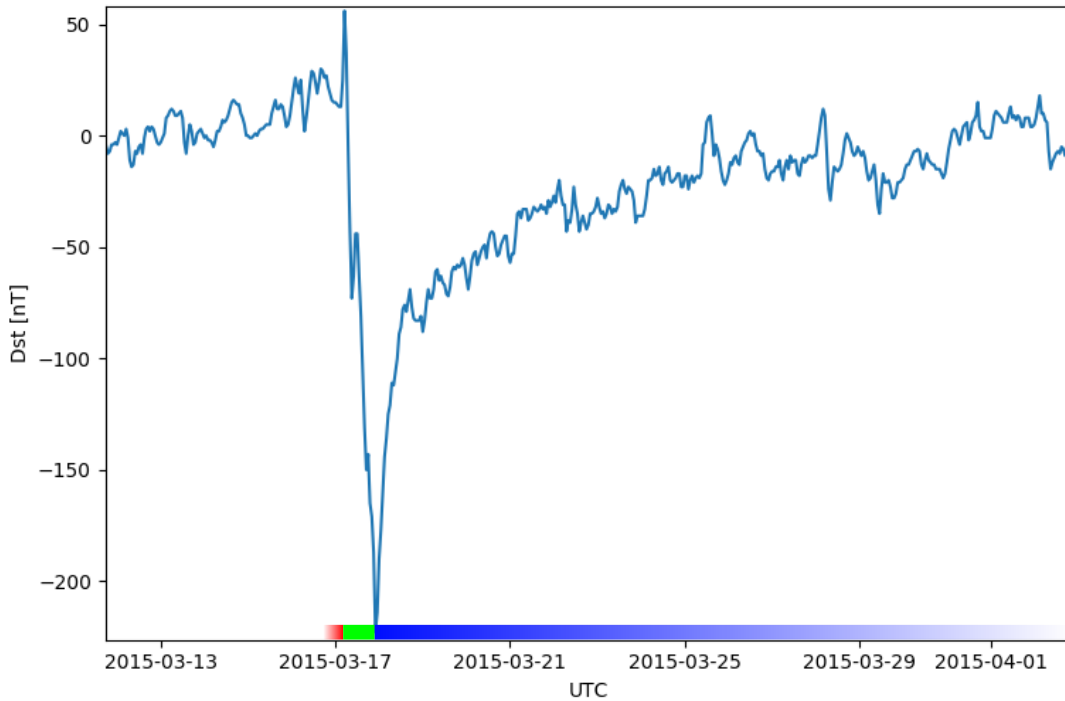


Figure 1.8: The DST index during the St. Patrick's Day 2015 storm. This storm was caused by a coronal mass ejection on March 15th, 2015. The storm phases are: initial phase, main phase, and recovery phase. The initial phase occurred when the Dst peaked at +50 nT on March 17th during which the ring current was eroded by the coronal mass ejection during the interval shown by the red bar. Then the rapid decrease to  $\approx -200$  nT was during the main phase where many injections from the magnetotail pumped up the ring current which reduced Earth's magnetic field strength at the ground and is shown with the green bar. Lastly, the recovery phase lasted from March 18th to approximately March 29th during which the ring current particles were lost and the ring current returned to its equilibrium state. The recovery phase is shown with the blue bar.

## The Earth's Electron Radiation Belts

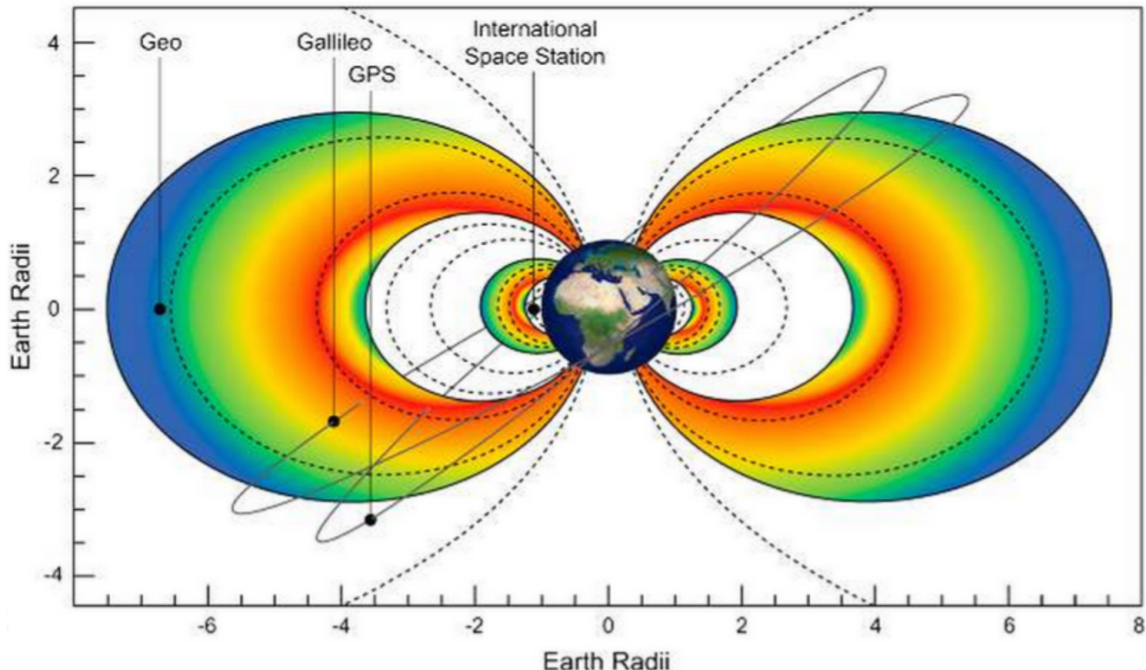


Figure 1.9: The two radiation belts with the locations of various satellites and orbits. Figure from (Horne et al., 2013).

<sup>181</sup> Radiation Belts The highest energy particle populations are in the Van Allen  
<sup>182</sup> radiation belts. These belts were discovered by Van Allen (1959) and Vernov and  
<sup>183</sup> Chudakov (1960) during the Cold War and are a pair of toroidally shaped populations  
<sup>184</sup> of trapped electrons and protons usually within to  $L < 8$  and are shown in Fig. 1.9.  
<sup>185</sup> Their quiescent toroidal shape is similar to the shape of the plasmasphere and ring  
<sup>186</sup> current and is a result of Earth's dipole magnetic field and the conservation of the  
<sup>187</sup> three adiabatic invariants discussed in section 1.

<sup>188</sup> The inner radiation belt is extremely stable on time periods of years, extends  
<sup>189</sup> to  $L \approx 2$ , and mainly consists of protons with energies between MeV and GeV and  
<sup>190</sup> electrons with energies up to  $\approx 1$  MeV (Claudepierre et al., 2019). The source of  
<sup>191</sup> inner radiation belt protons is believed to be due to cosmic-ray albedo neutron decay

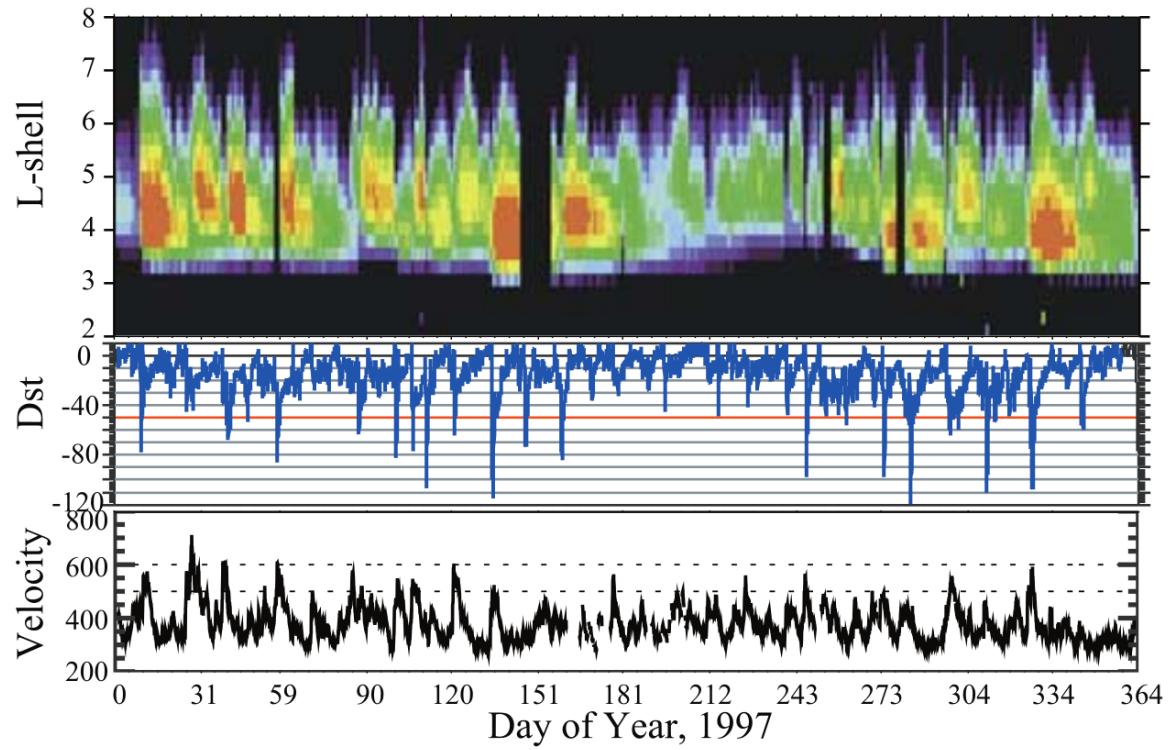


Figure 1.10: The dynamics of the outer radiation belt in 1997 from the POLAR satellite. Top panel shows the 1.2-2.4 MeV electron flux as a function of L and 1997 day of year. The middle panel shows the DST index, and bottom panel shows the solar wind velocity. Figure from (Reeves et al., 2003).

192 (e.g. Li et al., 2017) and inward radial diffusion for electrons (e.g. O'Brien et al.,  
 193 2016). The gap between the inner and outer radiation belt is called the slot, which is  
 194 believed to be due to hiss waves inside the plasmasphere (described below) scattering  
 195 particles into the atmosphere (e.g. Breneman et al., 2015; Lyons and Thorne, 1973).

196 The outer radiation belt, on the other hand is much more dynamic and consists  
 197 of mainly electrons of energies up to a few MeV. The outer belt's spatial extent is  
 198 highly variable e.g. see Fig. 1.10, and is typically observed at  $4 < L < 8$ . Since  
 199 the outer radiation belt contains a dynamic population of energetic particles that  
 200 pose a threat to human and technological presence in Earth's atmosphere and space,  
 201 decades of research has been undertaken to understand and predict the outer radiation  
 202 belt particles, waves, and wave-particle interactions. The dynamics of the outer  
 203 radiation belt can be understood by considering various competing acceleration and  
 204 loss mechanisms which will be described in the following sections.

205

### Radiation Belt Particle Sources and Sinks

206 Adiabatic Heating

207 One of the particle heating and transport mechanisms arises from the Earthward  
 208 convection of particles. The conservation of  $J_1$  implies that the initial and final  $v_\perp$   
 209 depends on the change in the magnetic field amplitude

$$\frac{v_{\perp i}^2}{B_i} = \frac{v_{\perp f}^2}{B_f}. \quad (1.12)$$

210 As a particle convects Earthward,  $B_f > B_i$  thus  $v_\perp$  must increase. The dipole  
 211 magnetic field amplitude can be written as

$$B(L, \theta) = \frac{31.2 \mu\text{T}}{L^3} \sqrt{1 + 3 \cos^2 \theta} \quad (1.13)$$

<sup>212</sup> which implies that

$$\frac{v_{\perp f}^2}{v_{\perp i}^2} = \left(\frac{L_i}{L_f}\right)^3. \quad (1.14)$$

<sup>213</sup> .

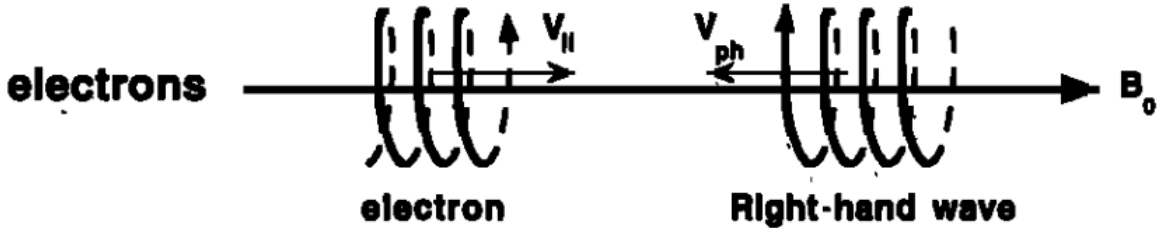
<sup>214</sup> In addition, as the particle convects Earthward the distance between the  
<sup>215</sup> particle's mirror points decrease. If  $J_2$  is conserved, the shrinking bounce path implies  
<sup>216</sup> that  $v_{||}$  must increase by

$$\frac{v_{|| f}^2}{v_{|| i}^2} = \left(\frac{L_i}{L_f}\right)^k \quad (1.15)$$

<sup>217</sup> where  $k$  ranges from 2 for equatorial pitch angles,  $\alpha_{eq} = 0^\circ$ , to 2.5 for  $\alpha_{eq} = 90^\circ$   
<sup>218</sup> (Baumjohann and Treumann, 1997). Since the rate of adiabatic heating is greater in  
<sup>219</sup> the perpendicular direction than heating in the parallel direction, an initially isotropic  
<sup>220</sup> particle distribution will become anisotropic during its convection. These isotropic  
<sup>221</sup> particles can then become unstable to wave growth and generate waves in order to  
<sup>222</sup> reach equilibrium.

### <sup>223</sup> Wave Resonance Heating

<sup>224</sup> Another mechanism that heats particles is due to particles resonating with  
<sup>225</sup> plasma waves. A few of the electromagnetic wave modes responsible for particle  
<sup>226</sup> acceleration (and deceleration) relevant to radiation belt dynamics are hiss, whistler  
<sup>227</sup> mode chorus (chorus), and electromagnetic ion cyclotron (EMIC) waves. These waves  
<sup>228</sup> are created by the loss cone instability that driven by an anisotropy of electrons  
<sup>229</sup> for chorus waves, and protons for EMIC waves. The level of anisotropy can be  
<sup>230</sup> quantified by the ratio of the perpendicular to parallel particle temperatures ( $T_{\perp}/T_{||}$ ).  
<sup>231</sup> A particle distribution is unstable when  $T_{\perp}/T_{||} > 1$  which facilitates wave growth.



$$\omega + k_{\parallel} v_{\parallel} = \Omega^-$$

Figure 1.11: The trajectories of an electron and a right-hand circularly polarized wave during a cyclotron resonance. The electron's  $v_{\parallel}$  and the wave's  $k_{\parallel}$  are in opposite directions such that the wave's frequency is Doppler shifted to an integer multiple of the electron cyclotron frequency. Figure from (Tsurutani and Lakhina, 1997).

232 Since electrons gyrate in a right-handed sense, the chorus waves also tend to be right  
 233 hand circularly polarized (Tsurutani and Lakhina, 1997). The same argument applies  
 234 to protons and left hand circularly polarized EMIC waves as well.

235 These circularly polarized waves can resonate with electrons and/or protons  
 236 when their combined motion results in a static  $\vec{E}$ . One example of a resonance  
 237 between a right hand circularly polarized wave and an electron is shown in Fig. 1.21  
 238 and is termed the cyclotron resonance. An electron's  $v_{\parallel}$  and the wave's parallel wave  
 239 vector,  $k_{\parallel}$  are in opposite directions such that the wave frequency  $\omega$  is Doppler shifted  
 240 to an integer multiple of the  $\Omega_e$  at which point the electron feels a static electric  
 241 field and is accelerated or decelerated. This acceleration happens when a resonance  
 242 condition is satisfied between a wave and a particle for which we will now derive an  
 243 illustrative toy model.

244 Assume a uniform magnetic field  $\vec{B} = B_0 \hat{z}$  with a parallel propagating ( $k = k\hat{z}$ ),  
 245 right-hand circularly polarized wave. The wave's electric field as a function of position  
 246 and time can be written as

$$\vec{E} = E_0 (\cos(\omega t - kz) \hat{x} + \sin(\omega t - kz) \hat{y}) \quad (1.16)$$

which is more clearly expressed by taking the dot product to find  $\vec{E}$  in the  $\hat{\theta}$  direction

$$E_\theta = \vec{E} \times \hat{\theta} = E_0 \cos(\omega t - kz + \theta). \quad (1.17)$$

<sup>247</sup> Now assume that the electron is traveling in the  $-\hat{z}$  direction with a velocity  $\vec{v} = -v_0 \hat{z}$   
<sup>248</sup> so its time dependent position along  $\hat{z}$  is

$$z(t) = -v_0 t \quad (1.18)$$

<sup>249</sup> and gyrophase is

$$\theta(t) = -\Omega t + \theta(0) \quad (1.19)$$

<sup>250</sup> where the first negative sign comes from the electron's negative charge. Now we put  
<sup>251</sup> this all together and express the electric field and the force that the electron will  
<sup>252</sup> experience

$$m \frac{dv_\theta}{dt} = qE_\theta = qE_0 \sin((\omega + kv_0 - \Omega)t + \theta(0)). \quad (1.20)$$

<sup>253</sup> This is a relatively complex expression, but when the time dependent component,

$$\omega + kv_0 - \Omega = 0, \quad (1.21)$$

<sup>254</sup> the electron will be in a static electric field which will accelerate or decelerate the  
<sup>255</sup> electron depending on  $\theta_0$ , the phase between the wave and the electron. **Show Bortnik  
<sup>256</sup> 2008 plot?** The expression in Eq. 1.21 is commonly referred to as the resonance

257 condition and is more generally written as

$$\omega - k_{||}v_{||} = \frac{n\Omega_e}{\gamma} \quad (1.22)$$

258 where  $n$  is the resonance order, and  $\gamma$  is the relativistic correction (e.g. Millan and  
259 Thorne, 2007). In the case of the cyclotron resonance,  $\omega \approx \Omega_e$  thus  $J_1$  is violated.  
260 Since  $J_1$  is violated,  $J_2$  and  $J_3$  are also violated since the conditions required to  
261 violate  $J_2$  and  $J_3$  are less stringent than  $J_1$ . It is important to remember that along  
262 the particle's orbit it will encounter and experience the effects of many waves along  
263 its orbit. The typical MLT extent of a handful of waves that are capable of resonating  
264 with radiation belt electrons are shown in Fig. 1.12.

265 Particle Losses

266 Now that we have seen two general mechanisms with which particles are  
267 accelerated and transported in the magnetosphere, we will now consider a few  
268 specific mechanisms with which particles are lost to the atmosphere or the solar  
269 wind. One particle loss mechanism into the solar wind is magnetopause shadowing  
270 (e.g. Ukhorskiy et al., 2006). Particles are sometimes lost when the ring current is  
271 strengthened and Earth's magnetic field strength is increased outside of the ring  
272 current (and reduced on Earth's surface). If the time scale of the ring current  
273 strengthening is slower than a particle drift,  $J_3$  is conserved. Then in order to  
274 conserve  $J_3$  while the magnetic field strength is increased, the particle's drift shell  
275 must move outward to conserve the magnetic flux contained by the drift shell. Then  
276 if the particle's drift shell expands to the point that it crosses the magnetopause, the  
277 particle will be lost to the solar wind.

278 **Move to acceleration?** Another particle loss and acceleration mechanism is driven  
279 by ultra low frequency (ULF) waves and is called radial diffusion. Radial diffusion is

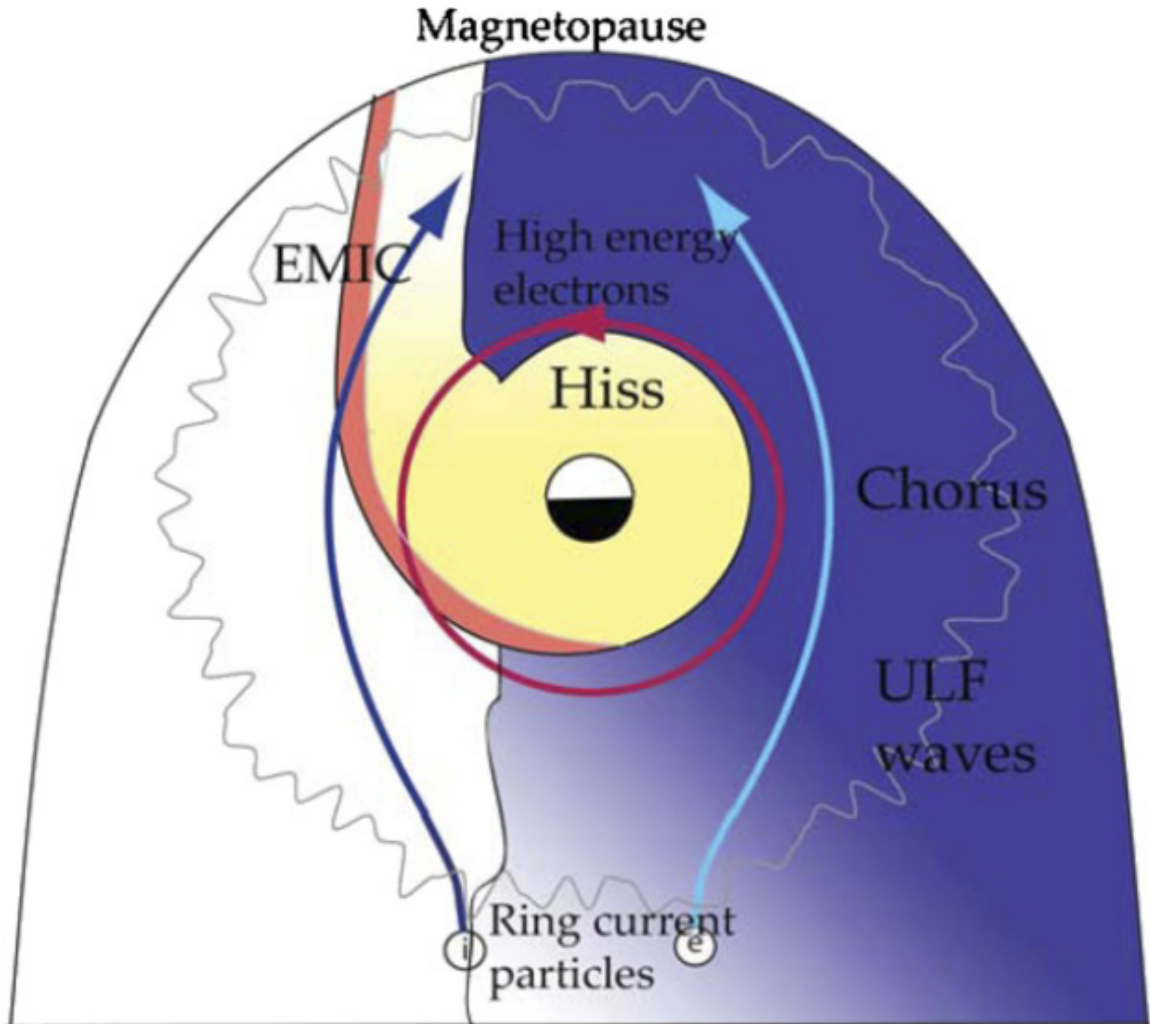


Figure 1.12: Various wave modes in the magnetosphere. Ultra low frequency waves occur through the magnetosphere. Chorus waves are typically observed in the 0-12 midnight-dawn region. EMIC waves are typically observed in the dusk MLT sector. Hiss waves are observed inside the plasmasphere. Figure from Millan and Thorne (2007).

280 the transport of particles from high to low phase space density,  $f$ . If the transport is  
 281 radially inward, particles will appear to be accelerated. On the other hand, radially  
 282 outward radial diffusion can transport particles through the magnetopause where  
 283 they will be lost to the solar wind. Reeves et al. (2013) investigated the driver of  
 284 particle acceleration during the October 2012 storm and observationally found that  
 285 inward radial diffusion was not dominant, rather local acceleration via wave-resonance  
 286 heating (i.e. particle diffusion in pitch angle and energy which will be described below)  
 287 appeared to be the dominant acceleration mechanism.

288 The loss mechanism central to this dissertation is pitch angle and energy  
 289 scattering of electrons by waves. Some of the waves that scatter electrons in energy  
 290 and pitch angle in the inner magnetosphere are: plasmaspheric hiss (e.g. Breneman  
 291 et al., 2015; O'Brien et al., 2014), EMIC waves (e.g. Capannolo et al., 2019; Hendry  
 292 et al., 2017), and chorus waves (e.g. Breneman et al., 2017; Kasahara et al., 2018;  
 293 Ozaki et al., 2019). These wave-particle interactions occur when the resonance  
 294 condition in Eq. 1.22 is satisfied at which point the particle's energy and  $\alpha$  is modified  
 295 by the wave. More details regarding the theory of pitch angle and energy diffusion is  
 296 given in Chapter X. If the wave changes  $\alpha$  towards 0 such that  $\alpha < \alpha_{LC}$ , the particle's  
 297 mirror point lowers to less than 100 km altitude where the particle can be lost due  
 298 collisions with air. One manifestation of pitch angle scattering of particles into the  
 299 loss cone are microbursts: a sub-second durtation impulse of electrons.

300

### Microbursts

301 Microbursts were first identified in high altitude balloon observations of bremsstrahlung  
 302 X-rays emitted by microburst electrons impacting the atmosphere by Anderson and  
 303 Milton (1964). Since then, other balloons have observed microburst X-ray signatures  
 304 in the upper atmosphere (e.g. Anderson et al., 2017; Barcus et al., 1966; Brown et al.,

305 1965; Parks, 1967; Trefall et al., 1966; Woodger et al., 2015). In addition to their X-ray  
 306 signature, microbursts electrons have been directly observed in LEO with spacecraft  
 307 including the Solar Anomalous and Magnetospheric Particle Explorer (SAMPEX),  
 308 Focused Investigation of Relativistic Electron Bursts: Intensity, Range, and Dynamics  
 309 II (FIREBIRD-II), Science Technologies Satellite (STSAT-I) (e.g. Blake et al., 1996;  
 310 Blum et al., 2015; Breneman et al., 2017; Crew et al., 2016; Lee et al., 2012, 2005;  
 311 Lorentzen et al., 2001a,b; Nakamura et al., 1995, 2000; O'Brien et al., 2004, 2003).  
 312 An example microburst time series is shown in Fig. 1.13 and was observed by  
 313 Montana State University's (MSU) FIREBIRD-II CubeSats. The prominent features  
 314 of microbursts in Fig. 1.13 are their  $\approx 1$  second duration, half order of magnitude  
 315 increase in count rate above the falling background, and their approximately 200-800  
 316 keV energy extent.

317 Microbursts are observed on magnetic field footprints that are connected to the  
 318 outer radiation belt (approximately  $4 < L < 8$ ), and are predominately observed in  
 319 the 0-12 MLT sector with an elevated occurrence frequency during magnetospherically  
 320 disturbed times as shown in Fig. 1.14. Microbursts have been previously observed  
 321 over a wide energy range from a few tens of keV (Datta et al., 1997; Parks, 1967) to  
 322 greater than 1 MeV (e.g. Blake et al., 1996; Greeley et al., 2019). The microburst  
 323 electron flux ( $J$ ) falls off in energy, and the microburst energy spectra is typically  
 324 well fit to a decaying exponential

$$J(E) = J_0 e^{-E/E_0} \quad (1.23)$$

325 where  $J_0$  is the flux at 0 keV (unphysical free parameter) and  $E_0$  quantifies the  
 326 efficiency of the scattering mechanism in energy (.e.g Datta et al., 1997; Lee et al.,  
 327 2005; Parks, 1967). A small  $E_0$  suggests that mostly low energy particles are scattered

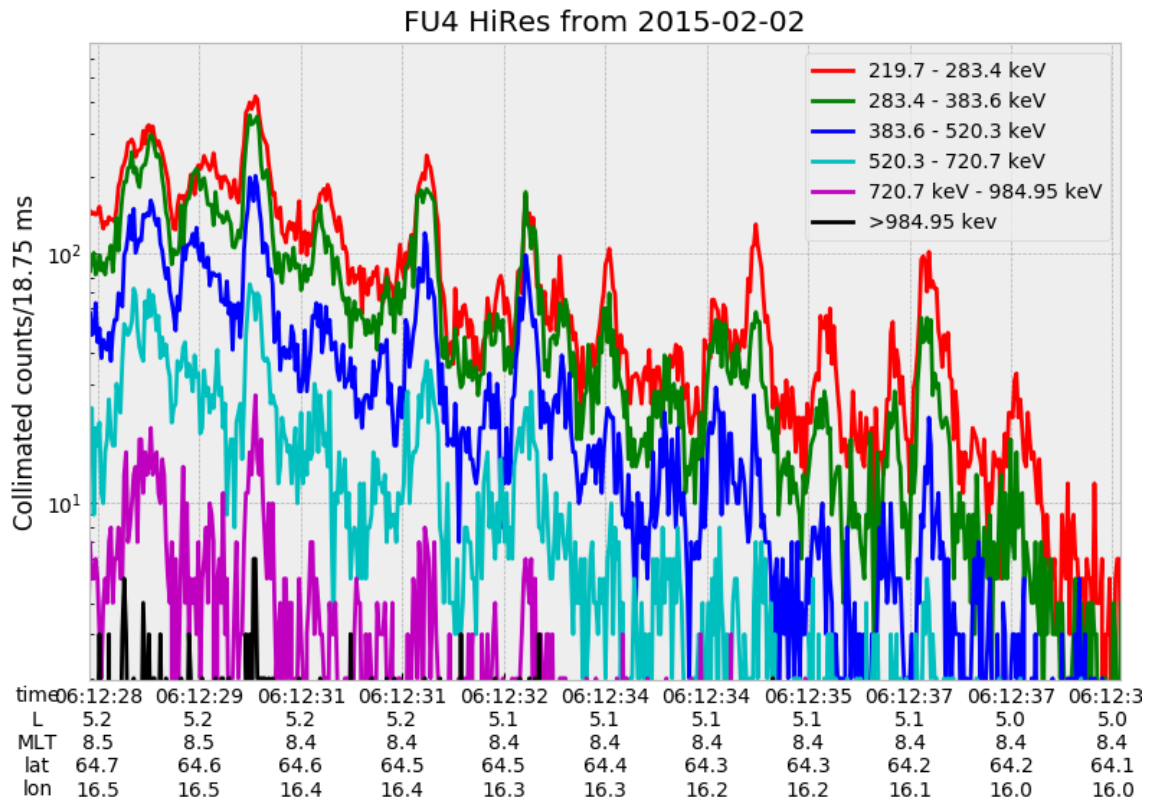


Figure 1.13: An example train of microbursts observed by FIREBIRD-II unit 4 on February 2nd, 2015. The colored curves show the differential energy channel count rates in six channels from  $\approx 200$  keV to greater than 1 MeV. The x-axis labels show auxiliary information such as time of observation and the spacecraft position in L, MLT, latitude and longitude coordinates.

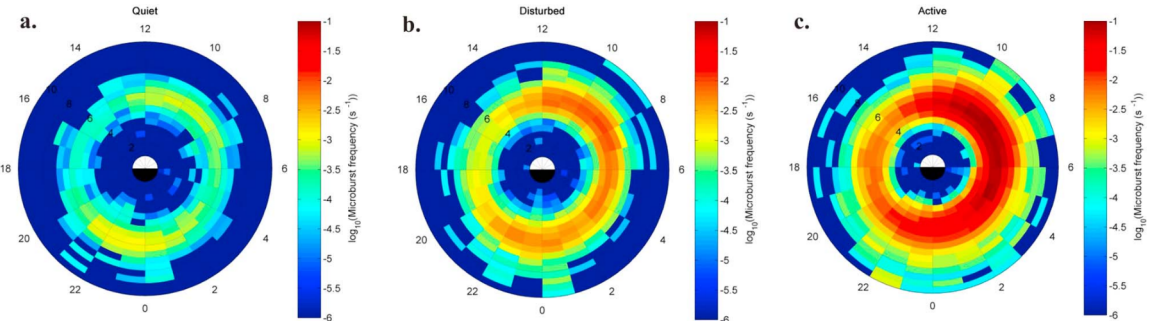


Figure 1.14: Relativistic ( $> 1\text{MeV}$ ) distribution of microburst occurrence rates as a function of L and MLT. The three panels show the microburst occurrence rate dependence on geomagnetic activity, parameterized by the auroral electrojet (AE) index for (a)  $\text{AE} < 100 \text{nT}$ , (b)  $100 < \text{AE} < 300 \text{nT}$  and (c)  $\text{AE} > 300 \text{nT}$ . Figure from Douma et al. (2017).

and a high  $E_0$  suggests that the scattering mechanism scatters low and high energy electrons. Reality is a bit more messy and a high  $E_0$  may be a signature of a scattering mechanism preferential to high energy electrons, but is hidden by the convolution of the source particles available to be scattered (typically with a falling energy spectrum) and the energy-dependent scattering efficiency.

The short duration of microbursts observed by a single LEO satellite has an ambiguity when interpreting what is exactly a microburst. The two possible realities are: a microburst is very small and spatially stationary so that the LEO spacecraft passes through it in less than a second. Alternatively, microbursts are spatially large with a short duration such that the microburst passes by the spacecraft in a fraction of a second. There are a few ways to distinguish between the two possible realities, and each one has a unique set of advantages.

A high altitude balloon provides essentially a stationary view of the precipitating particles under the radiation belt footprints so a short-lived, temporal microburst can be unambiguously identified. Spatial structures on the other hand are difficult to identify because a balloon is essentially still on drift timescales thus a variation in

344 the X-rays can be due to the spatial structure or an increase of precipitating particles  
 345 over the whole area. Furthermore, if the stationary structure is drifting its particles  
 346 are not precipitating into the atmosphere so there is no X-ray signature.

347 Another solution is multi-spacecraft missions that can determine if a microburst  
 348 is spatial or temporal. As will be shown in this dissertation, if a microburst is  
 349 observed simultaneously by two spacecraft then it is temporally transient and has  
 350 a size greater than the spacecraft separation. On the other hand, if two spacecraft  
 351 observe a microburst-like feature in the same location and at different times, then it is  
 352 spatial may be a curtain (Blake and O'Brien, 2016). Both observational methods have  
 353 a unique set of strengths, and this dissertation takes the multi-spacecraft approach  
 354 to identify and study microbursts.

355

### Scope of Reserach

356 This dissertation furthers our understanding of the microburst scattering  
 357 mechanism by observing the scattering directly, and measuring the microburst sizes  
 358 and comparing them to the size of waves near the magnetic equator where those  
 359 electrons could have been scattered. Chapter **X** describes a microburst scattering  
 360 event observed by NASA's Van Allen Probes which was studied in the theoretic  
 361 framework of pitch angle and energy diffusion. The following two chapters will then  
 362 study the size of microbursts. Chapter **Y** describes a bouncing packet microburst  
 363 observation made by MSU's FIREBIRD-II mission where the microburst's lower  
 364 bound longitudinal and latitudinal sizes were estimated. Then Chapter **Z** expands  
 365 the case study from Ch. **Y** to a statistical study of microburst sizes using The  
 366 Aerospace Corporation's AeroCube-6 (AC6) CubeSats. In this study, a Monte Carlo  
 367 and analytic microburst size models were developed to account for the compounding  
 368 effects of random microburst sizes and locations. Lastly, Ch. **A** will summarize the

<sub>369</sub> dissertation work and make concluding remarks regarding outstanding questions in  
<sub>370</sub> microburst physics.

## Bibliography

- 372 Anderson, B., Shekhar, S., Millan, R., Crew, A., Spence, H., Klumpar, D., Blake, J.,  
 373 O'Brien, T., and Turner, D. (2017). Spatial scale and duration of one microburst  
 374 region on 13 August 2015. *Journal of Geophysical Research: Space Physics*.
- 375 Anderson, K. A. and Milton, D. W. (1964). Balloon observations of X rays in the  
 376 auroral zone: 3. High time resolution studies. *Journal of Geophysical Research*,  
 377 69(21):4457–4479.
- 378 Barcus, J., Brown, R., and Rosenberg, T. (1966). Spatial and temporal character of  
 379 fast variations in auroral-zone x rays. *Journal of Geophysical Research*, 71(1):125–  
 380 141.
- 381 Baumjohann, W. and Treumann, R. A. (1997). *Basic space plasma physics*. World  
 382 Scientific.
- 383 Blake, J.,Looper, M., Baker, D., Nakamura, R., Klecker, B., and Hovestadt, D.  
 384 (1996). New high temporal and spatial resolution measurements by sampex of the  
 385 precipitation of relativistic electrons. *Advances in Space Research*, 18(8):171 – 186.
- 386 Blake, J. B. and O'Brien, T. P. (2016). Observations of small-scale latitudinal  
 387 structure in energetic electron precipitation. *Journal of Geophysical Research: Space  
 388 Physics*, 121(4):3031–3035. 2015JA021815.
- 389 Blum, L., Li, X., and Denton, M. (2015). Rapid MeV electron precipitation as  
 390 observed by SAMPEX/HILT during high-speed stream-driven storms. *Journal of  
 391 Geophysical Research: Space Physics*, 120(5):3783–3794. 2014JA020633.
- 392 Breneman, A., Crew, A., Sample, J., Klumpar, D., Johnson, A., Agapitov, O.,  
 393 Shumko, M., Turner, D., Santolik, O., Wygant, J., et al. (2017). Observations  
 394 directly linking relativistic electron microbursts to whistler mode chorus: Van allen  
 395 probes and FIREBIRD II. *Geophysical Research Letters*.
- 396 Breneman, A. W., Halford, A., Millan, R., McCarthy, M., Fennell, J., Sample, J.,  
 397 Woodger, L., Hospodarsky, G., Wygant, J. R., Cattell, C. A., et al. (2015). Global-  
 398 scale coherence modulation of radiation-belt electron loss from plasmaspheric hiss.  
 399 *Nature*, 523(7559):193.
- 400 Brown, R., Barcus, J., and Parsons, N. (1965). Balloon observations of auroral zone  
 401 x rays in conjugate regions. 2. microbursts and pulsations. *Journal of Geophysical  
 402 Research (U.S.)*.
- 403 Capannolo, L., Li, W., Ma, Q., Shen, X.-C., Zhang, X.-J., Redmon, R., Rodriguez,  
 404 J., Engebretson, M., Kletzing, C., Kurth, W., et al. (2019). Energetic electron  
 405 precipitation: multi-event analysis of its spatial extent during emic wave activity.  
 406 *Journal of Geophysical Research: Space Physics*.

- 407 Claudepierre, S., O'Brien, T., Looper, M., Blake, J., Fennell, J., Roeder, J.,  
 408 Clemmons, J., Mazur, J., Turner, D., Reeves, G., et al. (2019). A revised look  
 409 at relativistic electrons in the earth's inner radiation zone and slot region. *Journal*  
 410 *of Geophysical Research: Space Physics*, 124(2):934–951.
- 411 Crew, A. B., Spence, H. E., Blake, J. B., Klumpar, D. M., Larsen, B. A., O'Brien,  
 412 T. P., Driscoll, S., Handley, M., Legere, J., Longworth, S., Mashburn, K.,  
 413 Mosleh, E., Ryhajlo, N., Smith, S., Springer, L., and Widholm, M. (2016). First  
 414 multipoint in situ observations of electron microbursts: Initial results from the  
 415 NSF FIREBIRD II mission. *Journal of Geophysical Research: Space Physics*,  
 416 121(6):5272–5283. 2016JA022485.
- 417 Datta, S., Skoug, R., McCarthy, M., and Parks, G. (1997). Modeling of microburst  
 418 electron precipitation using pitch angle diffusion theory. *Journal of Geophysical*  
 419 *Research: Space Physics*, 102(A8):17325–17333.
- 420 Douma, E., Rodger, C. J., Blum, L. W., and Clilverd, M. A. (2017). Occurrence  
 421 characteristics of relativistic electron microbursts from SAMPEX observations.  
 422 *Journal of Geophysical Research: Space Physics*, 122(8):8096–8107. 2017JA024067.
- 423 Dungey, J. W. (1961). Interplanetary magnetic field and the auroral zones. *Phys.*  
 424 *Rev. Lett.*, 6:47–48.
- 425 Greeley, A., Kanekal, S., Baker, D., Klecker, B., and Schiller, Q. (2019). Quantifying  
 426 the contribution of microbursts to global electron loss in the radiation belts. *Journal*  
 427 *of Geophysical Research: Space Physics*.
- 428 Hendry, A. T., Rodger, C. J., and Clilverd, M. A. (2017). Evidence of sub-mev  
 429 emic-driven electron precipitation. *Geophysical Research Letters*, 44(3):1210–1218.
- 430 Horne, R., Glauert, S., Meredith, N., Boscher, D., Maget, V., Heynderickx, D., and  
 431 Pitchford, D. (2013). Space weather impacts on satellites and forecasting the earth's  
 432 electron radiation belts with spacecast. *Space Weather*, 11(4):169–186.
- 433 Horne, R. B., Thorne, R. M., Shprits, Y. Y., Meredith, N. P., Glauert, S. A., Smith,  
 434 A. J., Kanekal, S. G., Baker, D. N., Engebretson, M. J., Posch, J. L., et al.  
 435 (2005). Wave acceleration of electrons in the van allen radiation belts. *Nature*,  
 436 437(7056):227.
- 437 Kasahara, S., Miyoshi, Y., Yokota, S., Mitani, T., Kasahara, Y., Matsuda, S.,  
 438 Kumamoto, A., Matsuoka, A., Kazama, Y., Frey, H., et al. (2018). Pulsating  
 439 aurora from electron scattering by chorus waves. *Nature*, 554(7692):337.
- 440 Lee, J. J., Parks, G. K., Lee, E., Tsurutani, B. T., Hwang, J., Cho, K. S., Kim, K.-H.,  
 441 Park, Y. D., Min, K. W., and McCarthy, M. P. (2012). Anisotropic pitch angle  
 442 distribution of 100 keV microburst electrons in the loss cone: measurements from  
 443 STSAT-1. *Annales Geophysicae*, 30(11):1567–1573.

- 444 Lee, J.-J., Parks, G. K., Min, K. W., Kim, H. J., Park, J., Hwang, J., McCarthy,  
 445 M. P., Lee, E., Ryu, K. S., Lim, J. T., Sim, E. S., Lee, H. W., Kang, K. I., and  
 446 Park, H. Y. (2005). Energy spectra of 170–360 keV electron microbursts measured  
 447 by the korean STSAT-1. *Geophysical Research Letters*, 32(13). L13106.
- 448 Li, X., Selesnick, R., Schiller, Q., Zhang, K., Zhao, H., Baker, D. N., and Temerin,  
 449 M. A. (2017). Measurement of electrons from albedo neutron decay and neutron  
 450 density in near-earth space. *Nature*, 552(7685):382.
- 451 Lorentzen, K. R., Blake, J. B., Inan, U. S., and Bortnik, J. (2001a). Observations  
 452 of relativistic electron microbursts in association with VLF chorus. *Journal of  
 453 Geophysical Research: Space Physics*, 106(A4):6017–6027.
- 454 Lorentzen, K. R.,Looper, M. D., and Blake, J. B. (2001b). Relativistic electron  
 455 microbursts during the GEM storms. *Geophysical Research Letters*, 28(13):2573–  
 456 2576.
- 457 Lyons, L. R. and Thorne, R. M. (1973). Equilibrium structure of radiation belt  
 458 electrons. *Journal of Geophysical Research*, 78(13):2142–2149.
- 459 Millan, R. and Thorne, R. (2007). Review of radiation belt relativistic electron losses.  
 460 *Journal of Atmospheric and Solar-Terrestrial Physics*, 69(3):362 – 377.
- 461 Nakamura, R., Baker, D. N., Blake, J. B., Kanekal, S., Klecker, B., and Hovestadt,  
 462 D. (1995). Relativistic electron precipitation enhancements near the outer edge of  
 463 the radiation belt. *Geophysical Research Letters*, 22(9):1129–1132.
- 464 Nakamura, R., Isowa, M., Kamide, Y., Baker, D., Blake, J., and Looper, M. (2000).  
 465 Observations of relativistic electron microbursts in association with VLF chorus.  
 466 *J. Geophys. Res*, 105:15875–15885.
- 467 O'Brien, T., Claudepierre, S., Blake, J., Fennell, J. F., Clemons, J., Roeder, J.,  
 468 Spence, H. E., Reeves, G., and Baker, D. (2014). An empirically observed pitch-  
 469 angle diffusion eigenmode in the earth's electron belt near  $l^* = 5.0$ . *Geophysical  
 470 Research Letters*, 41(2):251–258.
- 471 O'Brien, T., Claudepierre, S., Guild, T., Fennell, J., Turner, D., Blake, J., Clemons,  
 472 J., and Roeder, J. (2016). Inner zone and slot electron radial diffusion revisited.  
 473 *Geophysical Research Letters*, 43(14):7301–7310.
- 474 O'Brien, T. and Moldwin, M. (2003). Empirical plasmapause models from magnetic  
 475 indices. *Geophysical Research Letters*, 30(4).
- 476 O'Brien, T. P., Looper, M. D., and Blake, J. B. (2004). Quantification of relativistic  
 477 electron microburst losses during the GEM storms. *Geophysical Research Letters*,  
 478 31(4). L04802.

- 479 O'Brien, T. P., Lorentzen, K. R., Mann, I. R., Meredith, N. P., Blake, J. B., Fennell,  
 480 J. F., Looper, M. D., Milling, D. K., and Anderson, R. R. (2003). Energization of  
 481 relativistic electrons in the presence of ULF power and MeV microbursts: Evidence  
 482 for dual ULF and VLF acceleration. *Journal of Geophysical Research: Space  
 483 Physics*, 108(A8).
- 484 Ozaki, M., Miyoshi, Y., Shiokawa, K., Hosokawa, K., Oyama, S.-i., Kataoka, R.,  
 485 Ebihara, Y., Ogawa, Y., Kasahara, Y., Yagitani, S., et al. (2019). Visualization of  
 486 rapid electron precipitation via chorus element wave-particle interactions. *Nature  
 487 communications*, 10(1):257.
- 488 Parks, G. K. (1967). Spatial characteristics of auroral-zone X-ray microbursts. *Journal  
 489 of Geophysical Research*, 72(1):215–226.
- 490 Reeves, G., Spence, H. E., Henderson, M., Morley, S., Friedel, R., Funsten, H., Baker,  
 491 D., Kanekal, S., Blake, J., Fennell, J., et al. (2013). Electron acceleration in the  
 492 heart of the van allen radiation belts. *Science*, 341(6149):991–994.
- 493 Reeves, G. D., McAdams, K. L., Friedel, R. H. W., and O'Brien, T. P. (2003). Ac-  
 494 celeration and loss of relativistic electrons during geomagnetic storms. *Geophysical  
 495 Research Letters*, 30(10):n/a–n/a. 1529.
- 496 Schulz, M. and Lanzerotti, L. J. (1974). *Particle Diffusion in the Radiation Belts*.  
 497 Springer.
- 498 Trefall, H., Bjordal, J., Ullaland, S., and Stadsnes, J. (1966). On the extension of  
 499 auroral-zone x-ray microbursts. *Journal of Atmospheric and Terrestrial Physics*,  
 500 28(2):225–233.
- 501 Tsurutani, B. T. and Lakhina, G. S. (1997). Some basic concepts of wave-particle  
 502 interactions in collisionless plasmas. *Reviews of Geophysics*, 35(4):491–501.
- 503 Turner, D., Claudepierre, S., Fennell, J., O'Brien, T., Blake, J., Lemon, C.,  
 504 Gkioulidou, M., Takahashi, K., Reeves, G., Thaller, S., et al. (2015). Energetic  
 505 electron injections deep into the inner magnetosphere associated with substorm  
 506 activity. *Geophysical Research Letters*, 42(7):2079–2087.
- 507 Ukhorskiy, A. Y., Anderson, B. J., Brandt, P. C., and Tsyganenko, N. A. (2006).  
 508 Storm time evolution of the outer radiation belt: Transport and losses. *Journal of  
 509 Geophysical Research: Space Physics*, 111(A11):n/a–n/a. A11S03.
- 510 Van Allen, J. A. (1959). The geomagnetically trapped corpuscular radiation. *Journal  
 511 of Geophysical Research*, 64(11):1683–1689.
- 512 Vernov, S. and Chudakov, A. (1960). Investigation of radiation in outer space. In  
 513 *International Cosmic Ray Conference*, volume 3, page 19.

- 514 Woodger, L., Halford, A., Millan, R., McCarthy, M., Smith, D., Bowers, G., Sample,  
515 J., Anderson, B., and Liang, X. (2015). A summary of the BARREL campaigns:  
516 Technique for studying electron precipitation. *Journal of Geophysical Research: Space Physics*, 120(6):4922–4935.  
517